Solutes that reduce yield strength anisotropies in magnesium from first principles

Michael R. Fellinger,[1] Louis G. Hector, Jr.,[2] and Dallas R. Trinkle[1,*]

[1]*Department of Materials Science and Engineering, University of Illinois at Urbana-Champaign, Urbana, Illinois 61801, USA*

[2]*General Motors Global R&D Center, 30470 Harley Earl Blvd., Warren, Michigan 48092, USA*

(Received 28 September 2021; accepted 11 November 2021; published 14 January 2022)

Using Labusch-type solid solution strengthening models parameterized with DFT-computed solute-dislocation interaction energies, we perform a computational search for 63 solutes across the periodic table to find those that lower anisotropy ratios (non-basal to basal CRSS) of magnesium potentially increasing its ductility per the von Mises criterion. For this purpose, we compute changes in strength for solutes as a function of composition and temperature, and compute anisotropy ratios for solutes that include both rare earth and non-rare earth elements. We specifically focus on solute-dislocation interaction energies in the following DFT-optimized dislocations as representative of three non-basal plastic deformation modes: $\langle c+a\rangle$ edge, $(10\bar{1}2)$ tension twinning edge, and the $(10\bar{1}1)$ compression twinning edge. We find that solute-induced changes in non-basal deformation modes can be approximated using a second-order polynomial in the size misfit of the solutes, which permits rapid screening of solutes. Our approach to identify solutes known to improve strengthening incorporates solute solubility, and suggests other solutes that not have been previously explored for strengthening. The 8 rare-earth solutes that our method suggests as the best, ordered by increasing anisotropy ratios at their optimal concentrations, are: Gd, Tb, Dy, Nd, Ho, Er, Tm, and Yb. The 12 non-rare-earth solutes that our method suggests as the best, ordered by increasing anisotropy ratios, are: Y, Mn, Sc, Pb, Ca, Ag, Bi, Tl, Zn, Li, Ga, and Al. Of these, Gd, Nd, Er, Yb, Y, Mn, Ca, Zn, Li, and Al are used in commercial Mg alloys.

DOI: 10.1103/PhysRevMaterials.6.013607

I. INTRODUCTION

Magnesium alloys have a high strength-to-weight ratio [1,2] and are therefore of interest to transportation industries as light weight alternatives to heavier non-ferrous and ferrous alloys. However, broader application of wrought Mg alloys in ground transportation vehicles, for example, has been limited by low room-temperature ductility, poor formability, and corrosion [3]. The low polycrystalline ductility is a result of the yield strength anisotropy of the HCP crystal structure of Mg. Slip activity is primarily limited to the basal plane at room temperature since the critical resolved shear stress (CRSS), or yield stress (these two terms are used interchangeably throughout), to move basal dislocations is more than an order-of-magnitude lower than the CRSS for non-basal deformation modes [4–10]. The large differences between the basal and non-basal CRSSs result in insufficient active slip systems at room temperature for generalized plasticity according to the von Mises criterion [11]; fracture occurs before plastic deformation and hence component forming requires application of heat to activate non-basal systems [12]. Room-temperature, non-basal plastic deformation modes in Mg are $(10\bar{1}2)$ twinning in tension [7,13], and $(10\bar{1}2)$ twinning and the slip of $\langle c+a\rangle$ dislocations in compression [10,14]. One approach to improving Mg plasticity is via solute additions to strengthen deformation modes, and reduce plastic anisotropy at lower temperatures. A useful metric is the ratios of the solute-induced non-basal CRSSs to the solute-induced basal CRSS: if a given solute lowers these for realistic solute solubilities in Mg, then improved plasticity will result.

Significant experimental and theoretical/computational research has focused on improving Mg alloy plasticity. Solid-solution strengthening using classical strengthening models parameterized with solute-dislocation interactions computed with density functional theory (DFT) has been the subject of several studies. For example, Yasi *et al.* [15,16] determined the strengthening potencies for many different solute species on basal dislocation slip [6] and thermally-activated basal to prismatic cross-slip in Mg alloys. Ghazisaeidi *et al.* [7] computed the strengthening effects of Al and Zn solutes on $(10\bar{1}2)$ tension twinning edge dislocations, and Buey *et al.* [10] performed similar strengthening calculations for Y solute on the slip of $\langle c+a\rangle$ edge dislocations. Jang *et al.* [17] recently developed a computational approach aimed at exploring activation of $\langle c+a\rangle$ slip in Mg alloys. Other studies have attempted to use surrogate quantities like generalized stacking fault energies to predict solute effects on non-basal slip in Mg alloys [18]. Experimental efforts have largely focused on the effects of alloying elements and processing on grain refinement [9,19–25] and texture modification [9,24–32], or introducing solutes [9,25,33,34], shaped precipitates [35–37], or long-period stacking ordered (LPSO) phases [38–40] to strengthen basal slip relative to non-basal deformation modes. These approaches are aimed at reducing the plasic anisotropy responsible for the poor room-temperature ductility of conventional Mg alloys.

*dtrinkle@illinois.edu

Recent experiments have led to new Mg alloys with improved room-temperature strength and ductility. Of particular note are the studies of Shi *et al.* [41,42], who developed Mg-2Zn-0.3Ca-0.2Ce-0.1Mn (wt%), a new Mg alloy with unprecedented room-temperature strength (∼269 MPa) and ductility (∼9.4%). These properties were achieved with a homogenization route designed with CALPHAD. Upon heat treatment, alloy ductility was substantially increased to ∼20% with a modest decrease in strength. The reported properties were attributed to a weakening of the basal texture, fine grain structure (nominal 5.4 μm), and Mn and $Mn_6Zn_3Ca_2$ precipitates. In a subsequent study, Shi *et al.* [42] used their experimental/computational approach to develop Mg-1.0Zn-1.0Al-0.5Ca-0.4Mn-0.2Ce (wt%) with a new homogenization route. This alloy has ∼31% ductility and ∼350 MPa strength at room temperature. Mechanical property improvements were attributed to a weak or split basal texture, a fine grain structure (nominal 9.6 μm), and formation of solute clusters. Zhou *et al.* [43] found that grain refinement and solid-solution strengthening are responsible for the considerable ductility of Mg-Sc-Yb-Mn-Zr alloys.

Despite impressive progress towards improving room-temperature mechanical properties, a fundamental study on the effects of a wide range of solutes on non-basal deformation in Mg is lacking. In particular, results from a comprehensive search across the periodic table to examine the effect of solute chemistry on the ratios of the solute-induced change in non-basal yield stresses to the solute-induced change in basal yield stress, while accounting for solute solubility, are not available. There is ample evidence in the literature that solutes such as Al, Zn, Ca, Mn, and various rare earth elements have a beneficial impact on Mg room-temperature mechanical properties but not necessarily via the same microstructural mechanisms [42]. Lithium, for example, is known to reduce the c/a ratio of Mg and activate non-basal slip while alteration of texture during recrystallization in Mg extrusion alloys has been attributed to Ce additions [44–46]. At present, the contribution from solute strengthening via interaction of solutes with dislocation cores on mechanical properties and its importance relative to other strengthening mechanisms are difficult to determine with experimental methods.

Here, we combine DFT calculations with solid solution strengthening models to explore the strengthening effect of 63 different solutes. We were especially interested to learn if our approach identifies solutes known to improve strengthening and if it suggests other solutes that not have been previously explored for strengthening. Solution strengthening in alloys is a direct consequence of solute interactions with dislocations [47], and electronic structure calculations are needed to compute these interactions accurately [6]. Therefore, we used density functional theory (DFT) to compute the interactions of selected solute species with three dislocation types associated with non-basal deformation in Mg: $\langle c+a\rangle$ edge, $(10\bar{1}2)$ tension twinning edge, $(10\bar{1}1)$ compression twinning edge. We use these direct interaction calculations to develop approximate interaction models that combine geometric information from the equilibrium dislocation cores in pure Mg with solute size and chemical misfits—quantities that can be efficiently computed with DFT. Labusch-type solution strengthening models previously applied to Y solutes in $\langle c+a\rangle$ edge dislocations [10] and Al and Zn solutes in $(10\bar{1}2)$ tension twinning edge dislocations in Mg [7] are employed. In addition to alleviating the high computational cost of calculating the solute-dislocation interactions by directly substituting every type of solute into all the sites of the three non-basal dislocation cores, the geometric models also quantify the relationships between the solute-dislocation interaction energies and solute misfits. The computed interaction energies parametrize the Labusch models, which predict changes to CRSS from 63 different solute species on the three different non-basal plastic deformation modes. We evaluate the potential of each solute to improve the strength and ductility of Mg by computing the ratios of the solute-induced change in non-basal CRSSs to the solute-induced change in basal CRSS. Promising solute candidates reduce these ratios thereby promoting dislocation slip on a larger number of slip systems required for generalized plastic deformation. Solute solubility is incorporated into the ratios.

II. COMPUTATIONAL METHODS

We determine the strengthening of 63 different substitutional solute species on $\langle c+a\rangle$ and $(10\bar{1}2)$ tension and $(10\bar{1}1)$ compression twinning edge dislocations in Mg using Labusch-type solid solution strengthening models [7,10,48,49]. The inputs to the strengthening models are (1) equilibrium dislocation core structures, which can determine (2) solute-dislocation interaction energies, along with (3) dislocation line tension. The dislocation core structures and solute interactions are all computed with density functional theory, while the line tension requires a empirical interatomic potential. As seen below, the Labusch model requires the interaction energy $U(x_i, y_i)$ of a solute at a variety of x_i, y_i positions within the dislocation core. Doing so directly requires a large number of computationally intense calculations. However, the direct calculations can be effectively replaced with a computationally simpler approach: the pure Mg defect geometries can be analyzed in terms of their local volumetric strain and local "slip" (in the pyramidal plane for $\langle c+a\rangle$, or the corresponding twin boundary for twin dislocations), and then the solute "misfit"—changes in lattice constants, stacking fault or twin energies—can be used to efficiently and accurately compute the interaction energy. Such an approach has a long history [6,7,10,16], and can be validated against the direct calculations. In addition, the interaction energy for solutes in different planes of a pyramidal fault or the two twin boundaries can *also* be effectively modeled as a quadratic function of the size misfit ϵ_v^s. While this is not possible for the basal fault—which has nearly zero elastic strain—the non-basal deformation modes all involve large local distortions with significant volumetric components. The end result is that the solute-dislocation interaction energies themselves are quite accurately expressible as quadratic functions of the solute size misfits, and so the strengthening models below can be rewritten in terms of the solute size misfits only. The Supplemental Material [50] contains additional details of the density functional theory calculations for line defects and the various solute misfits calculations, and the empirical models with respect to volumetric strain.

A. Solid-solution strengthening models

Labusch-type weak pinning models are used to calculate the effects of solute concentration, temperature, and strain rate on the critical resolved shear stress (CRSS) of the $\langle c+a\rangle$ edge dislocation, and $(10\bar{1}1)$ and $(10\bar{1}2)$ twinning edge dislocations. This approach has been previously applied to Y solutes with a $\langle c+a\rangle$ edge dislocation in Ref. [10], and for Al and Zn solutes with a $(10\bar{1}2)$ twinning edge dislocation in Ref. [7]. We briefly review the approach here. A dislocation bows out through a random field of solutes, taking on a shape that minimizes the combination of the solute-dislocation interaction energies and the elastic energy due to the change in the shape of the dislocation. The presence of solutes produces energy barriers that the dislocation must overcome to move through the lattice, thereby raising the yield stress. The total energy E_{tot} of the dislocation as a function of the dislocation bowing amplitude w and the bowed-out segment length ζ is

$$E_{\text{tot}}(\zeta, w) = \left[\left(\Gamma\frac{w^2}{2\zeta}\right) - \left(\frac{c_s\zeta}{a_0}\right)^{1/2}\Delta\widetilde{E}_p(w)\right]\frac{L}{2\zeta}, \quad (1)$$

where c_s is solute concentration, Γ is the dislocation line tension, L is the dislocation line length, and a_0 is the periodicity along the threading direction. The interaction with solutes enters through $\Delta\widetilde{E}_p(w)$; if we know the interaction energy $U(x_i, y_j)$ of a solute at position (x_i, y_j) relative to a dislocation centered at the origin with an xz slip plane, then the collective effect of all the solutes in Eq. (1) enters as

$$\Delta\widetilde{E}_p(w) = \left[\sum_{ij}\left(U(x_i, y_j) - U(x_i - w, y_j)\right)^2\right]^{1/2}. \quad (2)$$

Equation (1) can be analytically minimized with respect to ζ to find the characteristic segment length ζ_c; the characteristic width w_c is found via numerical minimization. From this, the zero-temperature change in yield stress $\Delta\tau_{y,0}$ is

$$\Delta\tau_{y,0} = \beta\left(\frac{c_s^2\Delta\widetilde{E}_p^4(w_c)}{\Gamma a_0^2 w_c^5}\right)^{1/3}, \quad (3)$$

where β is a unitless geometric factor related to the lattice geometry and slip system [10,49]. Including the effect of temperature T and strain rate $\dot{\epsilon}$ gives the change in stress required for dislocation motion $\Delta\tau_y$ is

$$\Delta\tau_y(T, \dot{\epsilon}) = \Delta\tau_{y,0}\left[1 - \left(\frac{T}{T_0}\right)^{2/3}\right], \quad (4)$$

where

$$T_0 = \frac{\alpha}{k_{\text{B}}\ln(\dot{\epsilon}/\dot{\epsilon_0})}\left(\frac{\Gamma w_c^2\Delta\widetilde{E}_p^2(w_c)c_s}{a_0}\right)^{1/3}, \quad (5)$$

and α is a unitless geometric factor similar to β and $\dot{\epsilon_0} = 10^5\text{s}^{-1}$ is a reference strain rate. The model of Eq. (4) is applicable directly for $\langle c+a\rangle$ strengthening.

However, as Ghazisaeidi *et al.* note, edge dislocations in twin boundaries act quite differently [7]. Namely, the term $E_{\text{tot}}(\zeta_c)$ does *not* reach a minimum with respect to w; rather, $E_{\text{tot}}/Lc_s^{2/3}$ approaches a constant limiting value. This is due to the interaction of solutes with the twin boundary itself, as opposed to the dislocation; motion of the dislocation necessarily moves solutes in and out of the twin boundary. In such a case, the model takes on a different, much simpler form [7],

$$\Delta\tau_y(T, \dot{\epsilon}) = \gamma\frac{[-E_{\text{tot}}/Lc_s^{2/3}]^{3/2}\sqrt{\Gamma}c_s}{k_{\text{B}}T\ln\dot{\epsilon_0}/\dot{\epsilon}}, \quad (6)$$

where the limiting value of $-E_{\text{tot}}/Lc_s^{2/3}$ is found numerically for a given solute, and γ is a unitless geometric factor related to the lattice geometry and twin system. References [7,10,51–53] provide additional details on the strengthening models. Determining the line tensions for our line defects requires the use of interatomic potentials as described in the Supplemental Material, and what remains is to determine the spatial distribution of solute-dislocation interaction energies $U(x_i, y_j)$ in and around the $\langle c+a\rangle$, $(10\bar{1}1)$ and $(10\bar{1}2)$ edge dislocations, which can be used in Eq. (4) and Eq. (6).

B. Solute interactions

The volumetric solute size misfit ϵ_V^s quantifies the size mismatch between the volume of solute atom s and the volume of a matrix Mg atom. The volumetric size misfit also determines the interaction energy of the solute with the volumetric strain field of defects like dislocations [6,7,10] and twin boundaries [54]. We compute volumetric size misfits for 63 substitutional solutes in Mg using the strain misfit tensor methodology in Refs. [55–57]. The strain misfit tensor ϵ_{ij}^s gives the derivative of solute-induced strain $e_{ij}^{c_s}$ with respect to solute concentration c_s. To determine ϵ_{ij}^s, we substitute a single substitutional solute into an HCP Mg supercell and then relax the positions of the atoms while keeping the supercell lattice vectors fixed. We then compute ϵ_{ij}^s from the solute's elastic dipole tensor P_{kl}^s and the DFT-computed elastic compliance tensor S_{ijkl}^0 of pure Mg,

$$\epsilon_{ij}^s = -\frac{1}{\Omega_0}\sum_{k,l}S_{ijkl}^0 P_{kl}^s, \quad (7)$$

where

$$P_{kl}^s = -N\Omega_0\sigma_{kl}^{(s,N,\Omega_0)}. \quad (8)$$

Here, Ω_0 is the volume per atom in the ideal solute-free HCP crystal, N is the number of lattice sites in the computational supercell, and $\sigma_{kl}^{(s,N,\Omega_0)}$ is the DFT-computed stress that a single solute induces in the supercell with fixed ideal HCP lattice vectors after relaxing the atomic positions. To ensure that only solute-induced stress is included in Eq. (8), any small residual stress in the solute-free supercell should be subtracted from $\sigma_{kl}^{(s,N,\Omega_0)}$. In the dilute limit, $\sigma_{kl}^{(s,N,\Omega_0)}$ scales with $1/N$ so P_{kl}^s becomes independent of supercell size. For substitutional solutes in Mg, ϵ_{ij}^s is diagonal. The element ϵ_{ii}^s gives the solute size misfit along Cartesian direction i, and the trace gives the volumetric size misfit ϵ_V^s.

The other misfits are defined in terms of the change in the fault energy (pyramidal stacking fault or twin fault energy), and depend on the position of the solute in the fault plane and distance away from it. For the pyramidal fault, it is

$$\epsilon_{\text{p2}}^{s,n} = \frac{1}{\gamma_{\text{p2}}}\left(\frac{\partial\gamma_{\text{p2}}}{\partial c_s}\bigg|_{c_s=0}\right)_n, \quad (9)$$

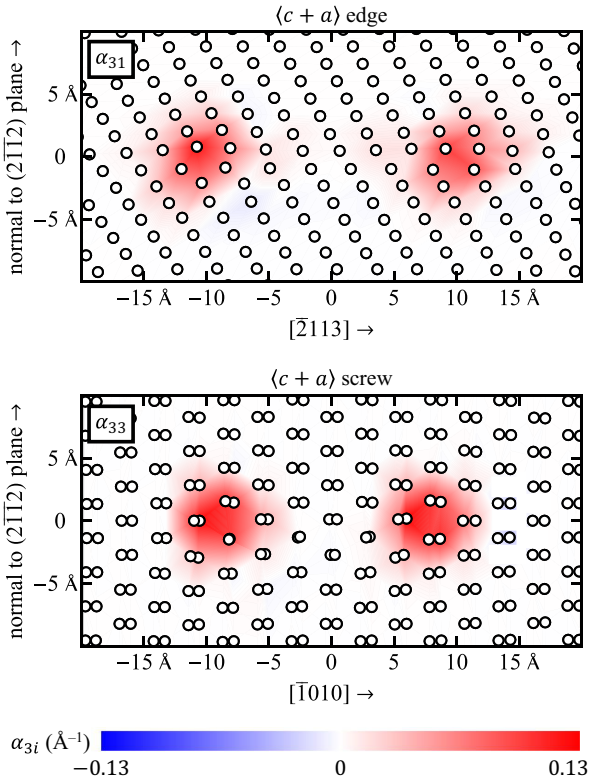

FIG. 1. Core structures of the $\langle c + a \rangle$ edge and screw dislocations optimized using DFT with LGF-based FBC. The edge core is visualized using the α_{31} edge component of the Nye tensor distributions, and the screw core is visualized using the α_{33} screw component. The dislocations dissociate into $1/2\langle c + a \rangle$ partial edge or screw dislocations separated by a pyramidal 2 stacking fault.

for layer n relative to the fault plane. It is worth noting that scaling by the fault energy to get a unitless quantity is purely convention for the "chemical misfit"; as we will use the misfit to construct an interaction energy model, we will have to multiply the misfit by the slip energy to produce an interaction energy. In a similar vein, we can compute the interaction energy, U_n, of a solute with respect to twin boundary for position n in the boundary; that is commonly reported simply as an interaction energy, and we do so here.

C. Effect of energy errors on $\Delta\tau_y$

As explained at the beginning of the methods section, we find we can accurately and efficiently reduce the prediction of strength changes to a simple model in terms of the solute size misfit ϵ_v^s; however, this introduces error in our prediction, and we wish to quantify this effect. We do so with a simple propagation of error approach; we compute the variance in $\Delta\tau_y$ from the variance and covariance in the interaction energies U_n,

$$\sigma^2_{\Delta\tau_y} = \sum_{m,n} \sigma^2_{U_m U_n} \left(\frac{\partial \Delta\tau_y}{\partial U_m}\right)\left(\frac{\partial \Delta\tau_y}{\partial U_n}\right), \tag{10}$$

where $\sigma^2_{U_m U_n}$ is the covariance matrix for the solute-dislocation interactions, and $\sigma^2_{U_m} \equiv \sigma^2_{U_m U_m}$ is the variance in U_m. We compute the covariance matrix $\sigma^2_{U_n,U_m}$ for the fault energies U_n

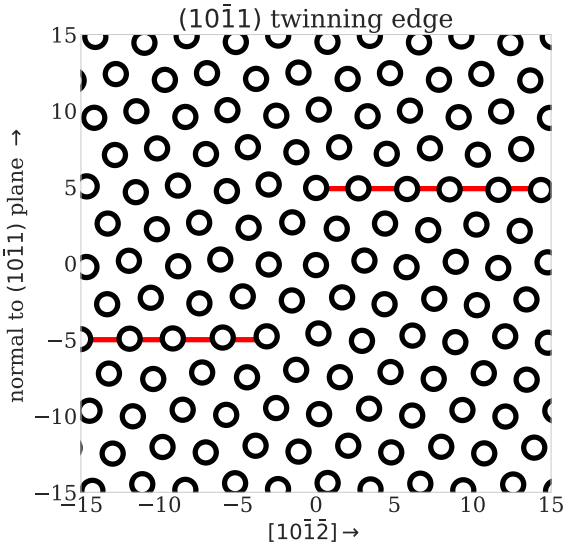

FIG. 2. Core structures of the $(10\bar{1}1)$ compression twinning edge dislocation optimized using DFT. The red lines indicate the two parallel twin planes, with the line defect spanning the distance between. The out-of-page direction is along the a direction.

using the direct and fitted solute-fault interactions,

$$\sigma^2_{U_n,U_m} = \frac{1}{N_s - 2} \sum_s \left(U_m^s - U_m^{s,\mathrm{fit}}\right)\left(U_n^s - U_n^{s,\mathrm{fit}}\right), \tag{11}$$

where N_s is the number of solutes used to fit the interactions as a function of solute size misfit, and $\sigma^2_{U_n} \equiv \sigma^2_{U_n,U_n}$.

III. RESULTS

Our intermediate goal is a prediction of the strength of different deformation modes, as a function of chemical composition, temperature and strain rate; from these, our final goal is the ratio of non-basal strengths to basal strengths to guide alloy selection. The strengthening models from Sec. II A require spatial interaction energies. For the $\langle c + a \rangle$ dislocation, that information starts with the pure Mg dislocation core structures; we can then directly substitute solutes at different sites. We find that knowing the local strain and slip in the pure core is sufficient to use a model for the interaction from *only* the size and stacking fault misfit; moreover, the stacking fault misfit *itself* can be well-approximated as a polynomial in the size misfit. For the $(10\bar{1}1)$ compression twin and $(10\bar{1}2)$ tension twin dislocations, the information starts with the pure Mg dislocation core structures *and* the twin boundaries; we can again directly substitute solutes at different sites for both the dislocation and the twin boundaries. We find that the changes in the twin boundary energies, and the interaction energies in the twin dislocation cores can be well-approximated as a polynomial in the size misfit. The final result is a model for the strength of different non-basal deformation modes in terms of the size misfit, solute concentration, temperature, and strain rate. The Supplemental Material [50] contains tabulated data for all of the fits in addition to the graphical data presented here.

TABLE I. Volumetric size misfits and approximate pyramidal 2 chemical misfits for 63 substitutional solutes in Mg. The chemical misfits are well-approximated by a second-order polynomial in the size misfit. The misfits are used to efficiently compute solute interactions with the different dislocations in this study, which ultimately lead to solid solution strengthening (see Fig. 7).

volumetric size misfit, ϵ_V^s

H																	He
Li −0.17	Be −0.72											B	C	N	O	F	Ne
Na 0.33	Mg											Al −0.34	Si −0.55	P	S	Cl	Ar
K 1.14	Ca 0.73	Sc 0.08	Ti −0.38	V −0.69	Cr −0.48	Mn −0.56	Fe −0.84	Co −1.13	Ni −1.01	Cu −0.77	Zn −0.44	Ga −0.34	Ge −0.38	As −0.37	Se	Br	Kr
Rb 1.47	Sr 1.18	Y 0.55	Zr −0.06	Nb −0.51	Mo −0.86	Tc −1.09	Ru −1.21	Rh −1.17	Pd −0.92	Ag −0.50	Cd −0.15	In 0.04	Sn 0.06	Sb 0.11	Te	I	Xe
Cs 1.71	Ba 1.55	*	Hf −0.11	Ta −0.53	W −0.89	Re −1.16	Os −1.31	Ir −1.31	Pt −1.12	Au −0.72	Hg −0.25	Tl 0.18	Pb 0.31	Bi 0.39	Po	At	Rn
*	La 0.98	Ce 0.92	Pr 0.84	Nd 0.78	Pm 0.73	Sm 0.69	Eu 0.94	Gd 0.61	Tb 0.57	Dy 0.54	Ho 0.51	Er 0.48	Tm 0.46	Yb 0.73	Lu		

pyramidal 2 chemical misfit, $\epsilon_{p2}^{s,1}$

H																	He
Li 0.03	Be 0.00											B	C	N	O	F	Ne
Na −0.09	Mg											Al 0.04	Si 0.03	P	S	Cl	Ar
K −0.55	Ca −0.27	Sc −0.02	Ti 0.04	V 0.01	Cr 0.03	Mn 0.03	Fe −0.02	Co −0.11	Ni −0.07	Cu 0.00	Zn 0.03	Ga 0.04	Ge 0.04	As 0.04	Se	Br	Kr
Rb −0.83	Sr −0.58	Y −0.18	Zr 0.01	Nb 0.03	Mo −0.03	Tc −0.09	Ru −0.14	Rh −0.13	Pd −0.04	Ag 0.03	Cd 0.02	In −0.01	Sn −0.01	Sb −0.02	Te	I	Xe
Cs −1.07	Ba −0.91	*	Hf 0.02	Ta 0.03	W −0.03	Re −0.12	Os −0.19	Ir −0.19	Pt −0.11	Au 0.00	Hg 0.03	Tl −0.04	Pb −0.08	Bi −0.11	Po	At	Rn
*	La −0.43	Ce −0.39	Pr −0.34	Nd −0.31	Pm −0.28	Sm −0.25	Eu −0.40	Gd −0.21	Tb −0.19	Dy −0.18	Ho −0.16	Er −0.15	Tm −0.14	Yb −0.28	Lu		

A. Dislocation core structures from first-principles calculations

The $\langle c+a \rangle$ edge and screw perfect dislocations dissociate into $1/2\langle c+a \rangle$ partial dislocations separated by a pyramidal 2 stacking fault. Figure 1 shows the dislocation geometries visualized using a combination of atomic positions and Nye tensor distributions [58,59]. Our core geometries relaxed using DFT with lattice Green function-based (LGF) flexible boundary conditions agree well with the DFT cores found in Refs. [60,61]. The screw dislocation core was optimized in Ref. [60] using LGF-based flexible boundary conditions, but the edge core in that work was optimized under fixed boundary conditions. The authors of Ref. [61] studied cross-slip mechanisms for screw dislocation using a periodic quadrupolar array configuration. The relaxed core structures provide substitutional sites for computing solute-dislocation interactions and geometric information used to construct computationally efficient approximations for these interaction energies. Our relaxed edge and screw geometries have substantially fewer atoms than previously published core structures, which greatly increases computational efficiency when computing solute-dislocation interactions by direct substitution of solutes into the core. We focus on solution strengthening of edge dislocations here, and leave strengthening of screw dislocation for a future study; it is expected that the strengthening effect of the screw dislocation will not be significantly different than that of the edge dislocation.

Figure 2 shows the computed $(10\bar{1}1)$ compression twinning edge dislocation, relaxed using DFT. Unlike the $\langle c+a \rangle$ dislocation cores, we use fixed boundary conditions to handle the dislocation core. The initial geometry is found using an modified-embedded atom potential [8], with a 50 000 atom geometry, then truncated to a 895 atom geometry; the outer 10 Å layer of atoms are held fixed. For the $(10\bar{1}2)$ tension twin edge dislocation, we use the relaxed geometry from [7].

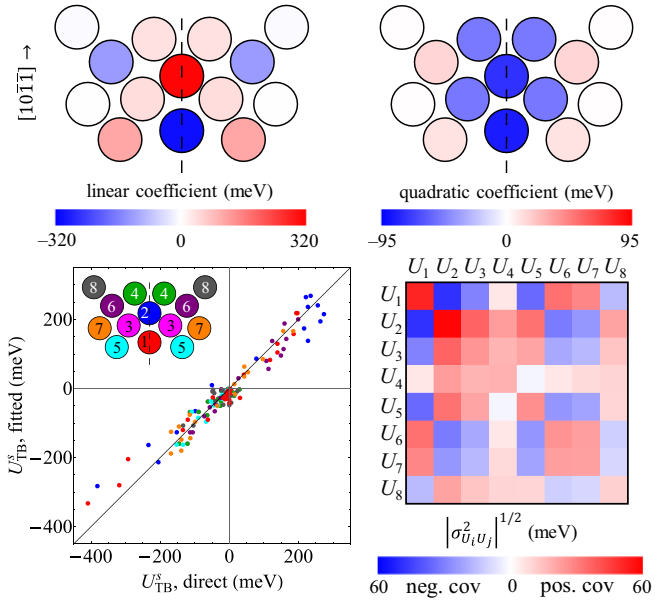

FIG. 3. Interaction energies of Al, Ba, Be, Ca, Cs, Ir, K, La, Li, Mn, Na, Os, Pr, Rb, Sn, Sr, Y, and Zn solutes with the (10$\bar{1}$2) tension twin boundary. (Top) The twin boundary is indicated by a dashed line in both left and right geometries; the sites on the left are colored based on the linear fitting coefficient $U^{(1)}$ for the solute interaction energies, while the right are colored based on the quadratic fitting $U^{(2)}$ coefficient. (Bottom left) The solute-twin boundary interaction energies computed from the polynomial (U^s_{TB}, fitted) agree with the directly computed interactions. The quadratic fits predict interaction energies for the other 45 solutes considered in this study. (Bottom right) The covariance matrix (visualized as a signed $|\sigma^2_{U_iU_j}|^{1/2}$) shows that the sites 1 and 2 have the largest fitting errors, and that these errors are anticorrelated; we can propagate these errors into our error estimates for our strengthening model [cf. Eqs. (6) and (10)].

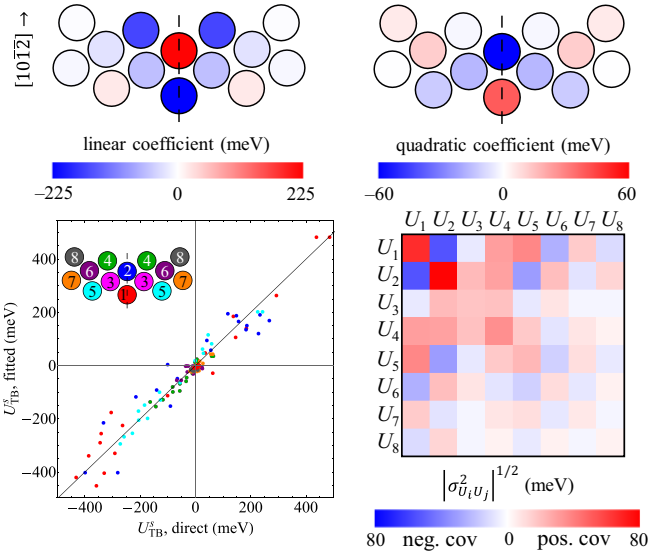

FIG. 4. Interaction energies of Al, Ba, Be, Ca, Cs, Ir, K, La, Li, Mn, Na, Os, Pr, Rb, Sn, Sr, Y, and Zn solutes with the (10$\bar{1}$1) compression twin boundary. (Top) The twin boundary is indicated by a dashed line in both left and right geometries; the sites on the left are colored based on the linear fitting coefficient $U^{(1)}$ for the solute interaction energies, while the right are colored based on the quadratic fitting $U^{(2)}$ coefficient. (Bottom left) The solute-twin boundary interaction energies computed from the polynomial (U^s_{TB}, fitted) agree with the directly computed interactions. The quadratic fits predict interaction energies for the other 45 solutes considered in this paper. (Bottom right) The covariance matrix (visualized as a signed $|\sigma^2_{U_iU_j}|^{1/2}$) shows that the sites 1 and 2 have the largest fitting errors; we can propagate these errors into our error estimates for our strengthening model [cf. Eqs. (6) and (10)].

B. Solute size and chemical misfits

Table I show our computed solute misfits of 63 different substitutional solute species in Mg using the strain misfit tensor approach discussed in Sec. II B. The size misfit ϵ^s_V shown in the top of Table I is the most significant quantity for our purposes, as the other changes in pyramidal slip and twin energies can be predicted using an approximation that is quadratic in the size misfit; the Supplemental Material [50] includes the quadratic equation. We computed pyramidal 2 chemical misfits for Al, Ca, Cs, Ir, K, La, Li, Mn, Na, Os, Pr, Rb, Sn, Sr, Y, and Zn solutes in the three atomic layers adjacent to the pyramidal 2 stacking fault (see Sec. II B). The volumetric size misfits ϵ^s_V of these solutes range from −1.31 for Os to 1.71 for Cs, and we find that the chemical misfits for all three layers are described well by a second order polynomial in ϵ^s_V. The polynomials provide a better description for solutes with positive ϵ^s_V than for solutes with negative ϵ^s_V, with the Os and Ir having the largest fitting errors. However, for solutes with large magnitude $|\epsilon^s_V|$, the solute-dislocation interactions are dominated by the volumetric strain contributions, and the slip energy contributions have a negligible effect on the strengthening predictions. We use the fitted dependence on ϵ^s_V to predict the chemical misfits for the rest of the solutes in this study. The values of the approximated chemical misfits for the 63 substitutional solutes are given in the bottom of Table I.

C. Solute-twin boundary interactions

For the interaction of solutes with twin boundaries, we computed direct interactions for 18 distinct solutes, then fit a second-order polynomial with size misfits to predict interactions for 63 solutes across the periodic table. For direct substitution, we chose the 18 solutes: Al, Ba, Be, Ca, Cs, Ir, K, La, Li, Mn, Na, Os, Pr, Rb, Sn, Sr, Y, and Zn. For both the (10$\bar{1}$1) compression and (10$\bar{1}$2) tension twin boundaries, we found that the interaction energies, $U^{s,\mathrm{fit}}_{n,\mathrm{TB}}$, can also be approximated in terms of the solute volumetric size misfit ϵ^s_V as

$$U^{s,\mathrm{fit}}_{n,\mathrm{TB}} := U^{(1)}_n \epsilon^s_V + U^{(2)}_n {\epsilon^s_V}^2, \tag{12}$$

where $U^{(1)}_n$ is the linear and $U^{(2)}_n$ the quadratic fitting parameters for each site n (the sites we consider are shown in Figs. 3 and 4, and Fig. S1 within the Supplemental Material [50]). These polynomials are used to predict the interactions of the other 45 solute species with the twin boundaries. The top panels of Figs. 3 and 4 show the linear and quadratic coefficients for each site in the (10$\bar{1}$1) and (10$\bar{1}$2) twin boundaries. The coefficients are largest at sites 1 and 2 in each boundary—those directly in the twin planes—and generally decrease in magnitude away from the boundaries,

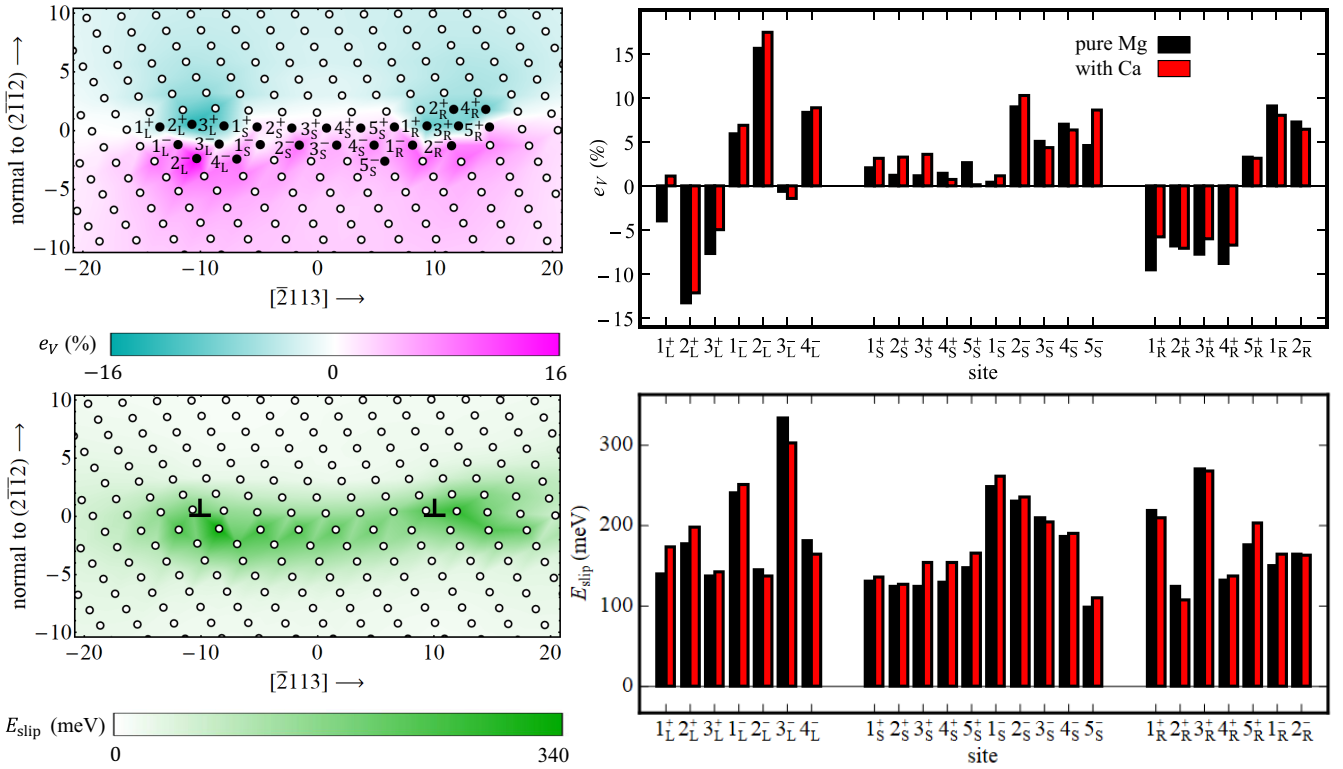

FIG. 5. Local volumetric strain e_V and slip energy E_{slip} distributions in the $\langle c+a \rangle$ edge dislocation core (sorted by strain). The figures on the left show the distributions for the pure Mg dislocation core and label 24 different sites in the core for direct solute substitution. The bar charts on the right show there are minimal changes in the strain and slip energy distributions after substituting a Ca solute at the sites in the equilibrium core.

showing that the solutes interact most strongly with sites 1 and 2. The bottom left panels of these two figures show the good agreement between the directly computed twin boundary interaction energies and the predicted energies from Eq. (12), which is quantified by the diagonal elements of the covariance matrices in the bottom right panels.

A recent study by Pei *et al.* [54] computed solute *segregation energies* for the two different sites in the (10$\bar{1}$2) and the (10$\bar{1}$1) twin boundaries (corresponding to sites 1 and 2 in the current paper) for 23 different solute species. Among the solutes they considered, Al, Be, La, Li, Os, Pr, Y, and Zn are common to our study. For these common solutes, our DFT-computed interaction energies for the (10$\bar{1}$2) agree with their DFT values to within 30 meV. Pei *et al.* also developed an approximation for solute-twin boundary interactions based on the solute size misfits and the local volumetric strain at each site in the boundaries computed using Voronoi volumes. Their model is linear in the size misfit, in contrast to our empirical models that contain terms that are linear and quadratic in the size misfit. In general, our predicted energies agree better with the direct DFT values due to the extra degree of freedom in our interaction models, compared with the approximation of Pei *et al.*

D. Solute-dislocation interactions from direct first-principles calculations

The interaction of solutes with the $\langle c+a \rangle$ edge dislocation can be described with an approximate geometric model, and validated against direct substitution of a Ca solute, as shown in Fig. 5. We substitute a single Ca solute into one of 24 different sites in the $\langle c+a \rangle$ dislocation core and compute the total energy of the system using DFT. We subtract a reference energy for a solute far from the dislocation cores from each of these energies to determine the interaction energy at each site. The geometric model of Eq. (S7) (see Supplemental Material [50]) expresses the energy as the sum of a volumetric energy (up to quadratic in size misfit) and a slip energy (linear in pyramidal 2 chemical misfit). The site-by-site analysis of the geometry is shown in Fig. 5, where we also investigate changes induced by the Ca solute; we find that there are only small changes in both the volumetric strain and local slip at each site, despite the large size misfit of a Ca atom, which suggests that using the pure Mg dislocation geometry is reliable. The bottom panel of Fig. 6 shows the agreement between the geometric and direct energy values, with a standard error of 70 meV. The effect of this error on the estimate of the solute strengthening in the Labusch model is shown below for Ca, and it is negligible.

We take a similar approach to the (10$\bar{1}$1) compression twinning edge dislocations, following the work of Ghazisaeidi *et al.* on the (10$\bar{1}$2) tension twinning edge dislocation [7]. The geometric model Eq. (S8) (see Supplemental Material [50]) is a sum of a volumetric strain term and chemical twinning misfit energy, with numerical values shown in Table II. The chemical twinning misfit energy is extracted from the solute interactions with pure twin boundaries, shown in Figs. 3 and 4; it, too, can be well-approximated as a quadratic function of the size misfit of different solutes, similar to Eq. (12). For the (10$\bar{1}$1)

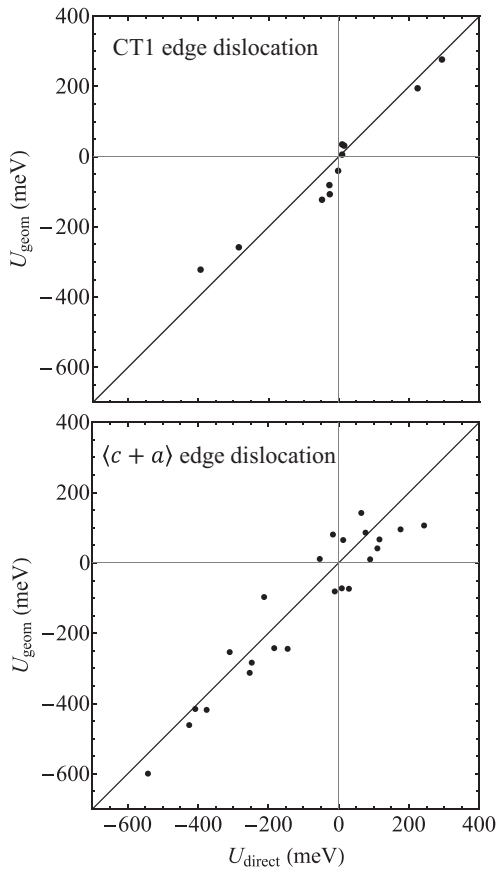

FIG. 6. Comparison of directly computed and geometric model interaction energies of a Ca solute with the $(10\bar{1}1)$ compression twinning edge dislocation (top) and the $\langle c+a\rangle$ edge dislocation (bottom). We computed the interactions U_{direct} at 12 different sites in the twinning dislocation core and at 24 different sites in the $\langle c+a\rangle$ dislocation core by direct substitution of a Ca solute into the different sites. We also compute these interactions using the geometric models for the twinning and $\langle c+a\rangle$ dislocations, Eq. (S8) and Eq. (S7) (see Supplemental Material [50]). The two sets of values agree well in each case, with variances of $\sigma_U = 45$ meV for the twinning dislocation and $\sigma_U = 70$ meV for the $\langle c+a\rangle$ dislocation.

compression twinning edge dislocations, we substitute a single Ca solute into one of 12 different sites and compute the total energy of the system using DFT. We subtract a reference energy for a solute far from the dislocation cores from each of these energies to determine the interaction energy at each site. The top panel of Fig. 6 shows the agreement between the geometric and direct energy values, with a standard error of 45 meV. The effect of this error on the estimate of the solute strengthening in the Labusch model is shown below for Ca, and it is negligible.

E. Solid-solution strengthening predictions for individual deformation modes

Figure 7 shows the accuracy of a simple model of strengthening for both twins and prismatic deformation with size misfit. We combine all of our interaction models—size and prismatic 2 chemical misfit, solute interactions with twin boundaries, and dislocation core interactions—with the Labusch strengthening of Eqs. (4) and (6) to predict the effect of solute chemistry and concentration on strength as a function of temperature and strain rate. In the end, due to the strong empirical correlation between size misfit and all of the interactions, the strength models can be ultimately reduced to a simple quadratic function of size misfit. The accuracy of this approximation can be seen clearly both in the fit (cf. Fig. 7) as well as the estimated variances, which give reasonable estimates of the errors. Our final empirical strengthening relations are

$$\left(\Delta\tau_y^s\right)_{\text{TT1}} = \frac{606 c_s/\text{at\%}}{(T/300\,\text{K})\{\ln[10^8] - \ln[\dot{\epsilon}/(10^{-3}\text{s}^{-1})]\}} \times {\epsilon_V^s}^2\,\text{MPa}, \tag{13}$$

$$\left(\Delta\tau_y^s\right)_{\text{CT1}} = \frac{1649 c_s/\text{at\%}}{(T/300\text{K})\{\ln[10^8] - \ln[\dot{\epsilon}/(10^{-3}\text{s}^{-1})]\}} \times {\epsilon_V^s}^2\,\text{MPa}, \tag{14}$$

$$\left(\Delta\tau_y^s\right)_{\langle\text{c+a}\rangle} = \{113(c_s/\text{at\%})^{2/3} - 1.84(T/300\,\text{K})^{2/3}(c_s/\text{at\%})^{4/9} \times (\ln[10^8] - \ln[\dot{\epsilon}/(10^{-3}\text{s}^{-1})])^{2/3}\}{\epsilon_V^s}^2\,\text{MPa}, \tag{15}$$

where T is the temperature and $\dot{\epsilon}$ is the strain rate. The variances, from Eq. (10), in each quantity *also* scale quadratically with the size misfit, and correspond to a less than 10% error for all predictions over the range of physically realizable size misfits.

F. Strength and ductility predictions for Mg alloys

Now with models of basal and non-basal strengths as functions of temperature and composition, we can reach our ultimate goal to suggest possible alloys with the lowest possible plastic anisotropy, for improved ductility and formability. In magnesium alloys, basal slip is easiest, and all additional modes of plastic deformation require higher stresses; at 300 K in *pure magnesium*, basal slip requires 1/6 of the stress to activate $(10\bar{1}2)$ tension twinning, 1/124 of the stress to activate $\langle c+a\rangle$ slip, and 1/200 of the stress to activate $(10\bar{1}1)$ compression twinning. The addition of solute elements strengthens all of these modes; however, as basal slip is an extremely easy deformation mode, adding solute elements can help reduce the plastic anisotropy associated with non-basal deformation modes, which in turn improves the ductility of magnesium alloys while increasing strength. We look to strike an important balance where we strengthen basal deformation significantly (to reduce plastic anisotropy) while not overly strengthening non-basal deformation (which would increase plastic anisotropy). As we saw in Sec. III E, strengthening increases quadratically with size misfits, but the modes respond quantitatively differently. However, as has been known since Hume-Rothery [62], solubility decreases with differences in atomic sizes; thus, we need to identify solutes with both a good balance of strengthening *and* solubility in magnesium that can aid in the design of improved alloys. Rather than rely on simple empirical relations for solubility, we turn to CALPHAD modeling, using the COST507 database [63] with the PYCALPHAD code [64] to find the *maximum* solubility for

TABLE II. Chemical twinning misfit energies for 63 substitutional solutes in the $(10\bar{1}2)$ tension twinning (TT1) and $(10\bar{1}1)$ compression twinning (CT1) dislocation cores in Mg. The misfits are used to efficiently compute solute interactions with the twinning dislocations, which ultimately lead to solid solution strengthening (see Fig. 7)

TT1 chemical misfit energy, ΔB^s_{chem} (meV)

−135 0 135

H																He
Li 1.1	Be −10.6											B	C	N	O	F	Ne
Na −8.6	Mg											Al 0	Si −4.4	P	S	Cl	Ar
K −65.0	Ca −29.9	Sc −1.3	Ti −0.5	V −9.1	Cr −2.5	Mn −4.7	Fe −16.2	Co −34.0	Ni −26.2	Cu −12.6	Zn −1.6	Ga 0.1	Ge −0.5	As −0.5	Se	Br	Kr
Rb −102.9	Sr −69.1	Y −18.9	Zr 0.6	Nb −3.3	Mo −17.5	Tc −31.1	Ru −40.1	Rh −37.1	Pd −20.5	Ag −3.1	Cd 1.1	In −0.6	Sn −0.9	Sb −1.9	Te	I	Xe
Cs −134.7	Ba −112.9	*	Hf 1.0	Ta −4.0	W −18.6	Re −36.3	Os −48.9	Ir −48.9	Pt −33.6	Au −10.7	Hg 0.8	Tl −3.6	Pb −7.7	Bi −11.1	Po	At	Rn
*	La −49.6	Ce −44.3	Pr −38.4	Nd −33.8	Pm −30.2	Sm −27.3	Eu −46.4	Gd −22.1	Tb −20.2	Dy −18.4	Ho −16.8	Er −15.4	Tm −14.1	Yb −30.4	Lu		

CT1 chemical misfit energy, ΔB^s_{chem} (meV)

−40 0 40

H																He
Li 0.3	Be −2.9											B	C	N	O	F	Ne
Na −2.4	Mg											Al 0	Si −1.2	P	S	Cl	Ar
K −17.8	Ca −8.2	Sc −0.3	Ti −0.1	V −2.5	Cr −0.7	Mn −1.3	Fe −4.4	Co −9.3	Ni −7.2	Cu −3.4	Zn −0.4	Ga 0.0	Ge −0.1	As −0.1	Se	Br	Kr
Rb −28.1	Sr −18.9	Y −5.2	Zr 0.2	Nb −0.9	Mo −4.7	Tc −8.5	Ru −11.0	Rh −10.1	Pd −5.6	Ag −0.9	Cd 0.3	In −0.2	Sn −0.3	Sb −0.5	Te	I	Xe
Cs −36.8	Ba −30.8	*	Hf 0.3	Ta −1.1	W −5.1	Re −9.9	Os −13.3	Ir −13.3	Pt −9.2	Au −2.9	Hg 0.23	Tl −1.0	Pb −2.1	Bi −3.0	Po	At	Rn
*	La −13.5	Ce −12.1	Pr −10.5	Nd −9.2	Pm −8.2	Sm −7.5	Eu −12.7	Gd −6.0	Tb −5.5	Dy −5.0	Ho −4.6	Er −4.2	Tm −3.9	Yb −8.3	Lu		

47 solutes (out of our 63) in magnesium; this often occurs at the solidus temperature, so quenching may be required to achieve this maximum. It should be noted that there are elements where the *optimal concentration*—defined as the concentration with the lowest ratio between $(10\bar{1}1)$ compression twinning and basal slip—is actually below the maximum solubility; this needs to be identified on a case-by-case basis.

Table III tabulates the best solutes for improving ductility, based on their possible reduction in plastic anisotropy (measured by plastic anisotropy ratios). In that table, we report the maximum solubility for each solute found in the COST507 database, as well as the optimal concentration; the optimal concentration is at the lowest possible ratio of compression twinning strength to basal strength at 300K *or* the maximum solubility, whichever is lowest. For each solute, we also report the change in strength at the optimal concentration for the three non-basal modes and basal deformation, as well the ratio of strengths. We have ordered the table from lowest ratio of $\tau_y^{\text{CT1}}/\tau_y^{\text{basal}}$ to largest with the rare earth solutes first, followed by the other solutes, to find the best 20 solutes *for which we have solubility data*. We choose to use the compression twinning to basal strength ratio to guide our selection as it is the largest anisotropy ratio at room temperature; moreover, we find that generally, this ratio remains larger than the pyramidal deformation or tension twin ratios. Thus, the solutes that reduce the $\tau_y^{\text{CT1}}/\tau_y^{\text{basal}}$ ratio also reduce the *other* non-basal anisotropy ratios. Not surprisingly, rare earth additions—well-known to improve the ductility and formability of magnesium alloys—are near the top. It should be noted that Y, Mn, Sc, Pb, and Ca are all competitive with rare earth solutes. We note that the solubilities of Sc, Tl, Li, and Al are large, which may result in less accurate quantitative strength predictions compared to elements with lower solubilities, as the strengthening models do not account for the effects of solute-solute interactions on the motion of the dislocation cores. Note also that Ce is not on our list; while Ce additions as little as 0.2 wt% are known to randomize Mg texture [46], which favors formability, all three anisotropy ratios are essentially unchanged relative to pure

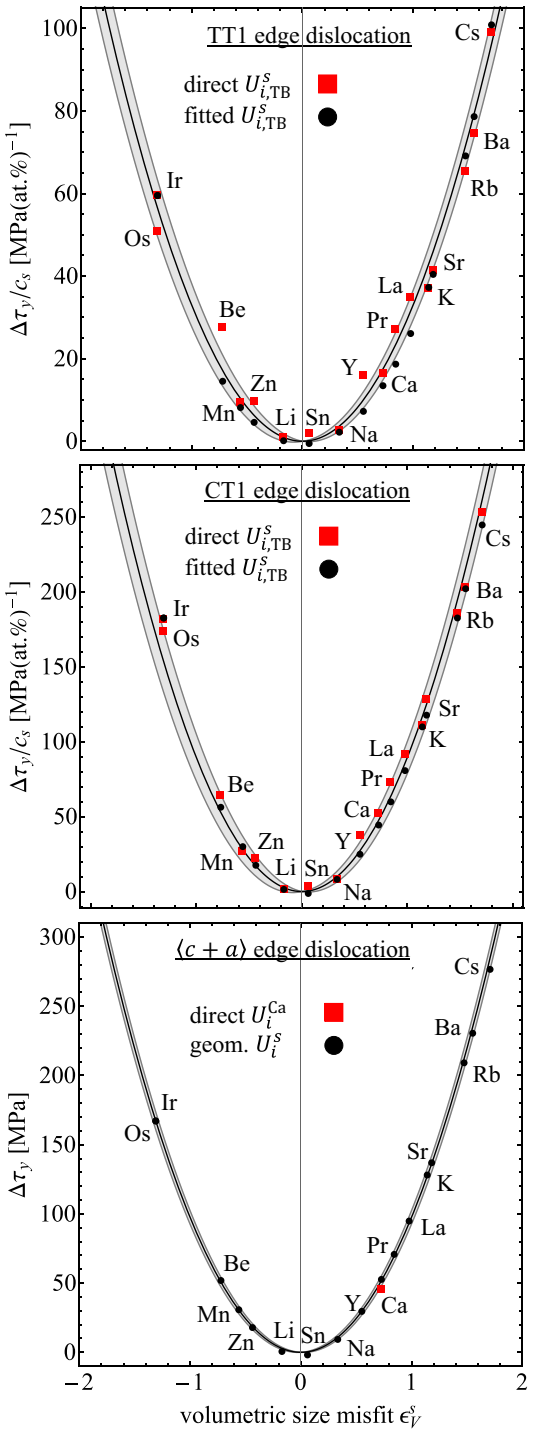

FIG. 7. Solute-induced change in τ_y for the $(10\bar{1}2)$ tension twinning, $(10\bar{1}1)$ compression twinning, and $\langle c+a\rangle$ edge dislocations for $T = 300$ K and $\dot{\epsilon} = 10^{-3}$ s^{-1}. The red squares are Labusch theory predictions for $\Delta\tau_y$ using directly computed solute-twin boundary interactions for the twinning dislocations, or direct solute-dislocation interactions for the $\langle c+a\rangle$ dislocation. The black points are Labusch predictions using fitted twin boundary interactions or geometric model interactions. As all of the interactions have been found to be well-approximated in terms of the size misfit, we find a simple quadratic scaling with the volumetric solute size misfit ϵ^s_V. The black curves are quadratic fits to the black points, and the shading corresponds to the predicted variance in $\Delta\tau_y$ computed from the variances in the solute-dislocation interaction energies (see Sec. II C). Like $\Delta\tau_y$, the variances also scale quadratically with the solute size misfit. The twinning strengthening is linear in concentration, while the $\langle c+a\rangle$ strengthening is evaluated for $c_s = 1$ at%. All non-basal modes show the largest strengthening for the largest magnitude size misfits.

Mg because of extremely low solubility in Mg up to 600 °C [65]. Our predictions are all predicated on a comparison of room-temperature anisotropies; as temperature is raised, the strength of the non-basal modes all decreases faster, permitting forming at very elevated temperatures, such as 300 °C. However, the solutes suggested by Table III should promote ductility and formability at lower temperatures, while also imparting increased strength to magnesium alloys. Combined with randomized texture, and possible precipitate strengthening, our results suggest possible paths to stronger and more ductile magnesium alloys.

IV. DISCUSSION AND CONCLUSION

Anisotropy ratios for three non-basal deformation modes in Mg relative to the basal deformation mode were computed for 63 potential strengthening solutes across the periodic table based upon Labusch-type solid solution strengthening models parameterized with DFT-computed solute-dislocation interaction energies. The three non-basal deformation modes were characterized by the $\langle c+a\rangle$ edge, $(10\bar{1}2)$ tension twinning edge, and the $(10\bar{1}1)$ compression twinning edge. The core structure of each dislocation was optimized to its equilibrium geometry with DFT and the flexible boundary condition approach. Due to the large computational cost of directly computing the interactions by directly substituting solutes into sites in the dislocation geometries, we developed computationally efficient approximations for the interactions that use geometric information from the geometries in pure Mg and solute size and chemical misfits. The size misfit quantifies the size mismatch between a solute and an HCP Mg atom, and the chemical misfit quantifies the interactions between solutes and stacking faults or twin boundaries. Both types of misfits were computed in supercells that are small compared to the dislocation supercells, providing a substantial computational savings compared to direct interaction calculations. We validated the approximate interaction energy models by comparing the energy predictions to a selected set of direct calculations for several different solute species. We find that both the interaction energies and the solute-induced changes in yield stress for the different non-basal dislocations scale as second order polynomials in the solute size misfit. These scaling relations provide a simple way to predict the strengthening potencies for a large number of different solute species in Mg. Strengthening potencies, which relate the solute-induced change in the CRSS to solute concentration, solute volumetric size misfit, temperature, and strain rate, were first computed. The solute-induced change in the CRSS predicts the increase in the energy barrier a dislocation must overcome to move under an applied load due to the balance between solute-dislocation interactions and the elastic energy of the dislocation, ultimately leading to an increase in yield stress

TABLE III. Solubilities, changes in yield stress $\Delta\tau_y$ for compression twinning (CT1), pyramidal deformation ($\langle c+a\rangle$), tension twinning (TT1), and basal deformation, and yield stress ratios for the 20 best solute species in Mg. The solubilities $c_s^{\max}$ are determined from the HCP boundaries of binary phase diagrams, and the optimal concentrations c_s^{opt} minimize the ratio $\tau_y^{\text{CT1}}/\tau_y^{\text{basal}}$. The solutes are divided into two groups: rare earth elements (upper group) and non-rare earth elements (lower group). The $\Delta\tau_y$ and $\tau_y^{\text{non-basal}}/\tau_y^{\text{basal}}$ values are evaluated at c_s^{opt}, $T = 300$ K and $\dot{\epsilon} = 10^{-3}\ \text{s}^{-1}$.

	[at%]		[MPa]						
solute	$c_s^{\max}$	c_s^{opt}	$\Delta\tau_y^{\text{CT1}}$	$\Delta\tau_y^{\langle c+a\rangle}$	$\Delta\tau_y^{\text{TT1}}$	$\Delta\tau_y^{\text{basal}}$	$\tau_y^{\text{CT1}}/\tau_y^{\text{basal}}$	$\tau_y^{\langle c+a\rangle}/\tau_y^{\text{basal}}$	$\tau_y^{\text{TT1}}/\tau_y^{\text{basal}}$
pure Mg							200	124	6
Gd	4.37	4.32	95.7	114.3	52.0	22.8	8.4	7.6	2.4
Tb	4.60	4.60	91.7	107.5	49.5	20.5	9.1	8.1	2.5
Dy	6.00	5.34	95.3	107.1	51.2	20.3	9.4	8.1	2.6
Nd	0.70	0.70	25.0	49.9	14.0	12.6	9.5	8.6	1.3
Ho	5.43	5.43	87.2	97.4	46.6	18.5	9.8	8.4	2.6
Er	6.05	6.05	87.2	94.4	46.4	18.3	10.0	8.3	2.6
Tm	2.31	2.31	30.1	42.1	15.9	11.9	10.5	8.4	1.5
Yb	0.67	0.67	21.3	42.7	11.8	8.4	13.7	11.8	1.7
Y	4.11	3.50	94.6	81.4	34.7	17.1	11.1	8.2	2.1
Mn	1.00	1.00	28.0	31.4	10.3	10.2	12.0	8.7	1.2
Sc	21.46	21.46	10.4	6.1	4.4	7.4	14.0	8.7	0.9
Pb	7.69	7.69	46.3	46.6	23.8	8.9	15.5	11.5	2.8
Ca	0.40	0.40	18.8	19.7	6.9	6.8	16.3	11.2	1.4
Ag	6.08	4.61	90.5	83.5	38.1	9.5	19.1	14.6	4.1
Bi	0.95	0.95	9.2	15.8	4.8	5.1	19.6	13.9	1.4
Tl	16.10	16.10	34.1	27.5	16.9	5.1	24.0	16.0	3.6
Zn	2.92	2.92	56.3	45.5	18.3	5.5	26.1	18.0	3.6
Li	17.70	17.70	56.4	27.0	17.0	4.9	28.7	16.3	3.7
Ga	3.24	3.24	27.8	29.0	11.9	3.7	30.1	21.5	3.5
Al	11.60	7.18	84.9	54.3	27.4	5.6	30.1	19.0	4.9

to move the dislocations relative to pure Mg. We also combine our solution strengthening predictions with CALPHAD predictions of solubility limits to suggest promising candidate solutes for improving the strength and ductility of Mg alloys. Solutes with the greatest potential for improving the mechanical properties of Mg alloys should strengthen the individual deformation modes, while reducing the plastic anisotropy of Mg by lowering the ratios of non-basal to basal yield stresses. We used the COST507 database for light metals and the PYCALPHAD code to compute the solubility limits in the HCP phase for twelve binary Mg alloys, and take the solubility limits of 35 other binary Mg alloys from literature. Our strengthening predictions show that solutes with large positive or large negative size misfits are most effective at increasing the yield stress of the different deformation modes. However, these solutes generally have low solubilities in HCP Mg so their overall effectiveness at improving the mechanical properties of Mg alloys is limited in practice. Solutes with small size misfits can have large solubilities in HCP Mg, but their strengthening potencies are small so they are also ineffective at improving mechanical properties. So a compromise that includes optimal solubility is needed. Any extra solute additions that lead to increased solubility of mid-sized solutes should also lead to improved Mg alloys. Further studies combining our solution strengthening data with phase diagram calculations using comprehensive databases on alloy thermodynamics could be performed to search for new multicomponent Mg systems with enhanced solubilities.

The major conclusions from this study are

(1) The 8 rare earth solutes that our method suggests as the best, ordered by the increasing anisotropy ratios at their optimal concentrations, are: Gd, Tb, Dy, Nd, Ho, Er, Tm, and Yb. Of these, Gd, Nd, Er, Yb are used in commercial alloys [66].

(2) The smallest and hence most favorable $\tau_y^{\text{CT1}}/\tau_y^{\text{basal}}$ anisotropy ratio for the rare earth solutes is 8.4 for Gd, while the largest is 13.7 for Yb. These represent considerable improvements in ductility relative to the value of 200 for pure Mg.

(3) The 12 non-rare earth solutes that our method suggests as the best, ordered by increasing anisotropy ratios, at their optimal concentrations, are: Y, Mn, Sc, Pb, Ca, Ag, Bi, Tl, Zn, Li, Ga, and Al. Of these, Y, Mn, Ca, Zn, Li, and Al are used in commercial Mg alloys [66].

(4) The smallest and hence most favorable $\tau_y^{\text{CT1}}/\tau_y^{\text{basal}}$ anisotropy ratio for the non-rare earth solutes is 11.1 for Y, while the largest is 30.1. These represent considerable improvements relative to the value of 200 for pure Mg.

(5) There is no need to exclusively use the computationally more expensive DFT to compute the solute/dislocation interaction energies when examining a large number of solutes. Rather, computationally efficient approximations for the interactions that use geometric information from the geometries in pure Mg and solute size and chemical misfits can be used at far less computational expense.

The VASP input and output files, along with all direct calculations for solute interactions are available to download at the LightMat DataHub [67].

ACKNOWLEDGMENTS

This material is based upon work supported by the Department of Energy National Energy Technology Laboratory under Award No. DE-EE0007756. The views expressed herein do not necessarily represent the views of the U.S. Department of Energy or the United States Government. The research was performed using computational resources provided by the National Energy Research Scientific Computing Center, the Department of Energy's Office of Energy Efficiency and Renewable Energy and located at the National Renewable Energy Laboratory, and the General Motors High Performance Computing Center.

[1] H. E. Friedrich and B. L. Mordike, *Magnesium Technology: Metallurgy, Design Data, Applications* (Springer-Verlag, Berlin, 2010).

[2] T. M. Pollock, Weight loss with magnesium alloys, Science **328**, 986 (2010).

[3] M. Zhang, L. G. Hector, Jr., Y. Guo, M. Liu, and L. Qi, First-principles search for alloying elements to increase corrosion resistance of Mg with Fe impurities, Comput. Mater. Sci. **165**, 154 (2018).

[4] S. R. Agnew and O. Duygulu, Plastic anisotropy and the role of non-basal slip in magnesium alloy, Int. J. Plast. **21**, 1161 (2005).

[5] W. B. Hutchinson and M. Barnett, Effective values of critical resolved shear stress for slip in polycrystalline magnesium and other hcp metals, Scr. Mater. **63**, 737 (2010).

[6] J. Yasi, L. G. Hector, Jr., and D. R. Trinkle, First-principles data for solid-solution strengthening of magnesium: From geometry and chemistry to properties, Acta Mater. **58**, 5704 (2010).

[7] M. Ghazisaeidi, L. G. Hector, Jr., and W. A. Curtin, Solute strengthening of twinning dislocations in Mg alloys, Acta Mater. **80**, 278 (2014).

[8] Z. Wu, M. F. Francis, and W. A. Curtin, Magnesium interatomic potential for simulating plasticity and fracture phenomena, Modell. Simul. Mater. Sci. Eng. **23**, 015004 (2015).

[9] K. K. Alaneme and E. A. Okotete, Enhancing plastic deformability of Mg and its alloys–A review of traditional and nascent developments, J. Mag. Alloys **5**, 460 (2017).

[10] D. Buey, L. G. Hector, Jr., and M. Ghazisaeidi, Core structure and solute strengthening of second-order pyramidal $\langle c+a \rangle$ dislocations in Mg-Y alloys, Acta Mater. **147**, 1 (2018).

[11] G. I. Taylor, Plastic strain in metals, J. Inst. Met. **62**, 307 (1938).

[12] A. Carpenter, A. Antoniswamy, J. T. Carter, L. G. Hector, Jr., and E. M. Taleff, A new magnesium AZ31 material constitutive model that accounts for grain growth and plastic anisotropy during hot deformation at 450 °C, Acta Mater. **68**, 254 (2014).

[13] J. R. Morris, Y. Ye, and M. H. Yoo, First-principles examination of the $(10\bar{1}2)$ twin boundary in hcp metals, Philos. Mag. **85**, 233 (2005).

[14] E. Lilleodden, Microcompression study of Mg (0001) single crystal, Scr. Mater. **62**, 532 (2010).

[15] J. Yasi, L. G. Hector, Jr., and D. R. Trinkle, Prediction of thermal cross-slip stress in magnesium alloys from direct first-principles data, Acta Mater. **59**, 5652 (2011).

[16] J. Yasi, L. G. Hector, Jr., and D. R. Trinkle, Prediction of thermal cross-slip stress in magnesium alloys from a geometric interaction model, Acta Mater. **60**, 2350 (2012).

[17] H.-S. Jang, J.-K. Lee, A.J.S.F. Tapia, N. Kim, and B.-J. Lee, Activation of $\langle c+a \rangle$ non-basal slip in multicomponent mg alloys, J. Magnes. Alloy. (to be published).

[18] Z. Ding, G. Zhao, H. Sun, S. Li, F. Ma, E. J. Lavernia, Y. Zhu, and W. Liu, Alloying effects on the plasticity of magnesium: Comprehensive analysis of influences of all five slip systems, J. Phys.: Condens. Matter **32**, 015401 (2019).

[19] T. Mukai, M. Yamanoi, H. Watanabe, and K. Higashi, Ductility enhancement in AZ31 magnesium alloy by controlling its grain structure, Scr. Mater. **45**, 89 (2001).

[20] W. J. Kim and H. T. Jeong, Grain-size strengthening in equal-channel-angular-pressing processed AZ31 Mg alloys with a constant texture, Mater. Trans. **46**, 251 (2005).

[21] W. J. Kim, H. G. Jeong, and H. T. Jeong, Achieving high strength and high ductility in magnesium alloys using severe plastic deformation combined with low-temperature aging, Scr. Mater. **61**, 1040 (2009).

[22] A. C. Hänzi, F. H. D. T. ans A. S. Sologubenko, P. Gunde, R. Schmid-Fetzer, M. Kuehlein, J. F. Löffler, and P. J. Uggowitzer, Design strategy for microalloyed ultra-ductile magnesium alloys, Philos. Mag. Lett. **89**, 377 (2009).

[23] Q. Yu, L. Qi, R. K. Mishra, J. Li, and A. M. Minor, Reducing deformation anisotropy to achieve ultrahigh strength and ductility in Mg at the nanoscale, Proc. Natl. Acad. Sci. USA **110**, 13289 (2013).

[24] L. Lu, C. Liu, J. Zhao, W. Zeng, and Z. Wang, Modification of grain refinement and texture in AZ31 Mg alloy by a new plastic deformation method, J. Alloys Compd. **628**, 130 (2015).

[25] J. D. Robson, Critical assessment 9: Wrought magnesium alloys, Mat. Sci. Tech. **31**, 257 (2015).

[26] J. Bohlen, M. R. Nürnberg, J. W. Senn, D. Letzig, and S. R.Agnew, The texture and anisotropy of magnesium-zinc-rare earth alloy sheets, Acta Mater. **55**, 2101 (2007).

[27] S. Suwas, G. Gottstein, and R.Kumar, Evolution of crystallographic texture during equal channel angular extrusion (ECAE) and its effects on secondary processing of magnesium, Mat. Sci. Eng.: A **471**, 1 (2007).

[28] L. W. F. Mackenzie and M. Pekguleryuz, The influences of alloying additions and processing parameters on the rolling microstructures and textures of magnesium alloys, Mater. Sci. Eng.: A **480**, 189 (2008).

[29] K. Hantzsche, J. Bohlen, J. Wendt, K. U. Kainer, S. B. Yi, and D. Letzig, Effect of rare earth additions on microstructure and texture development of magnesium alloy sheets, Scr. Mater. **63**, 725 (2010).

[30] T. Al-Samman and X.Li, Sheet texture modification in magnesium-based alloys by selective rare earth alloying, Mater. Sci. Eng. A **528**, 3809 (2011).

[31] S. H. Park, S.-G. Hong, and C. S. Lee, Enhanced stretch formability of rolled Mg-3Al-1Zn alloy at room temperature by initial $\{10\bar{1}2\}$ twins, Mater. Sci. Eng. A **578**, 271 (2013).

[32] Y. Zou, L. Zhang, H. Wang, X. Tong, M. Zhang, and Z. Zhang, Texture evolution and their effects on the mechanical properties of duplex Mg-Li alloy, J. Alloys Compd. **669**, 72 (2016).

[33] N. Tahreen, D. L. Chen, M. Nouri, and D. Y. Li, Influence of aluminum content on twinning and texture development of cast Mg-Al-Zn alloy during compression, J. Alloys Compd. **623**, 15 (2015).

[34] M. A. Kumar, I. J. Beyerlein, and C. N. Tomé, A measure of plastic anisotropy for hexagonal close packed metals: Application to alloying effects on the formability of Mg, J. Alloys Compd. **695**, 1488 (2017).

[35] J. F. Nie, Effects of precipitate shape and orientation on dispersion strengthening in magnesium alloys, Scr. Mater. **48**, 1009 (2003).

[36] N. Stanford, J. Geng, Y. B. Chun, C. H. J. Davies, J. F.Nie, and M. R. Barnett, Effect of plate-shaped particle distributions on the deformation behaviour of magnesium alloy AZ91 in tension and compression, Acta Mater. **60**, 218 (2012).

[37] J. D. Robson, N. Stanford, and M. R. Barnett, Effect of precipitate shape and habit on mechanical asymmetry in magnesium alloys, Metall. Mater. Trans. A **44A**, 2984 (2013).

[38] M. Matsuda, S. Ando, and M. Nishida, Dislocation structure in rapidly solidified $Mg_97Zn_1Y_2$ alloy with long period stacking order phase, Mater. Trans. **46**, 361 (2005).

[39] K. Hagihara, A. Kinoshita, Y.Sugino, M. Yamasaki, Y. Kawamura, H. Y. Yasuda, and Y. Umakoshi, Effect of long-period stacking ordered phase on mechanical properties of Mg97Zn1Y2 extruded alloy, Acta Mater. **58**, 6282 (2010).

[40] J. Shao, Z. Chen, T. Chen, Z. Hu, X. Zhou, and C. Liu, The effect of lpso on the deformation mechanism of Mg-Gd-Y-Zn-Zr magnesium alloy, J. Mag. Alloys **4**, 83 (2016).

[41] R. Shi, J. Miao, and A. A. Luo, A new magnesium sheet alloy and its multi-stage homogenization for simultaneously improved ductility and strength at room temperature, Scr. Metall. **171**, 92 (2019).

[42] R. Shi, J. Miao, T. Avery, and A. A. Luo, A new magnesium sheet alloy with high tensile properties and room temperature formability, Sci. Rep. **10**, 1044 (2020).

[43] T. Zhou, Z. Liua, D. Yanga, S. Menga, Z. Jiaa, and D. Liu, High ductility in solution-treated mg-sc-yb-mn-zr alloy mediated by $\langle c + a \rangle$ dislocations, J. Alloys Compds. **873**, 159880:1 (2021).

[44] R. Hooper, Z. L. Bryanm, and M. V. Manuel, The effect of indium additions on Mg-Li and Mg-Li-Al alloys, Metall. Mater. Trans. A **45**, 55 (2013).

[45] D. Christianson, L. Zhu, and M. V. Manuel, Experimental measurement of diffusion coefficients diffusion mobilities in HCP Mg-Li-Al alloys, Calphad **71**, 101999 (2020).

[46] R. K. Mishra, A. Gupta, P. R. Rao, A. K. Sachdev, A. M. Kumar, and A. A. Luo, Influence of cerium on texture and ductility of magnesium extrusions, Scr. Mater. **59**, 562 (2008).

[47] A. S. Argon, *Strengthening Mechanisms in Crystal Plasticity* (Oxford University Press, Oxford, 2008).

[48] G. P. M. Leyson and W. A. Curtin, Friedel vs. Labusch: The strong/weak pinning transition in solute strengthened metals, Philos. Mag. **93**, 2428 (2013).

[49] C. Varvenne, G. P. M. Leyson, M. Ghazisaeidi, and W. A. Curtin, Solute strengthening in random alloys, Acta Mater. **124**, 660 (2017).

[50] See Supplemental Material at http://link.aps.org/supplemental/10.1103/PhysRevMaterials.6.013607 for DFT computational details, and detailed derivations of all strengthening models, as well as additional details for calculations of line tensions and energies, which also includes Refs. [68–92].

[51] G. P. M. Leyson, L. G. Hector, Jr., W. A. Curtin, and C. Woodward, Quantitative prediction of solute strengthening in aluminium alloys, Nat. Mater. **9**, 750 (2010).

[52] G. P. M. Leyson, L. G. Hector, Jr., and W. A. Curtin, Solute strengthening from first principles and application to aluminum alloys, Acta Mater. **60**, 3873 (2012).

[53] G. P. M. Leyson, L. G. Hector, Jr., and W. A. Curtin, First-principles prediction of yield stress for basal slip in Mg-Al alloys, Acta Mater. **60**, 5197 (2012).

[54] Z. Pei, R. Li, J.-F. Nie, and J. R. Morris, First-principles study of the solute segregation in twin boundaries in Mg and possible descriptors for mechanical properties, Mat. Design **165**, 107574 (2019).

[55] M. R. Fellinger, L. G. Hector, Jr., and D. R. Trinkle, *Ab initio* calculations of the lattice parameter and elastic stiffness coefficients of bcc Fe with solutes, Comput. Mater. Sci. **126**, 503 (2017).

[56] M. R. Fellinger, L. G. Hector, Jr., and D. R. Trinkle, Effect of solutes on the lattice parameters and elastic stiffness coefficients of body-centered tetragonal Fe, Comput. Mater. Sci. **152**, 308 (2018).

[57] M. R. Fellinger, L. G. Hector, Jr., and D. R. Trinkle, Impact of solutes on the lattice parameters and elastic stiffness coefficients of hcp Fe from first-principles calculations, Comput. Mater. Sci. **164**, 116 (2019).

[58] C. S. Hartley and Y. Mishin, Representation of dislocation cores using Nye tensor distributions, Mater. Sci. Eng. A **400–401**, 18 (2005).

[59] C. S. Hartley and Y. Mishin, Characterization and visualization of the lattice misfit associated with dislocation cores,, Acta Mater. **53**, 1313 (2005).

[60] M. Ghazisaeidi, L. G. Hector, Jr., and W. A. Curtin, First-principles core structures of $\langle c + a \rangle$ edge and screw dislocations in Mg, Scr. Mater. **75**, 42 (2014).

[61] M. Itakura, H. Kaburaki, M. Yamaguchi, and T. Tsuru, Novel Cross-Slip Mechanism of Pyramidal Screw Dislocations in Magnesium, Phys. Rev. Lett. **116**, 225501 (2016).

[62] W. Hume-Rothery, R. W. Smallman, and C. W. Haworth, *The Structure of Metals and Alloys* (The Institute of Metals, London, 1969).

[63] I. Ansara, A. T. Dinsdale, and M. H. Rand (eds.), *COST 507 : Thermodynamical Database for Light Metal Alloys*, Vol. 2 (Office for Official Publications of the European Communities, Luxembourg, 1998).

[64] R. Otis and Z.-K. Liu, pycalphad: CALPHAD-based computational thermodynamics in python, J. Open Res. Software **5**, 1 (2017).

[65] L. L. Rohklin, Dependence of the rare earth metal solubility in solid magnesium on its atomic number, J. Phase Equilbira **19**, 142 (1998).

[66] A. A. Luo, Magnesium: The lightest structural metal, available at https://www.intlmag.org/page/mg-lightest-metal (2018).

[67] M. R. Fellinger, L. G. Hector, Jr., and D. R. Trinkle, Data citation: Density functional theory solute-dislocation interactions (2021), doi: 10.25584/1811899.

[68] G. Kresse and J. Furthmüller, Efficient iterative schemes for *ab initio* total-energy calculations using a plane-wave basis set, Phys. Rev. B **54**, 11169 (1996).
[69] J. P. Perdew, K. Burke, and M. Ernzerhof, Generalized Gradient Approximation Made Simple, Phys. Rev. Lett. **77**, 3865 (1996).
[70] P. E. Blöchl, Projector augmented-wave method, Phys. Rev. B **50**, 17953 (1994).
[71] G. Kresse and D. Joubert, From ultrasoft pseudopotentials to the projector augmented-wave method, Phys. Rev. B **59**, 1758 (1999).
[72] M. Methfessel and A. T. Paxton, High-precision sampling for Brillouin-zone integration in metals, Phys. Rev. B **40**, 3616 (1989).
[73] P. E. Blöchl, O. Jepsen, and O. K. Andersen, Improved tetrahedron method for Brillouin-zone integrations, Phys. Rev. B **49**, 16223 (1994).
[74] S. Vannarat, M. H. F. Sluiter, and Y. Kawazoe, First-principles study of solute dislocation interaction in aluminum-rich alloys, Phys. Rev. B **64**, 224203 (2001).
[75] B. Yin, Z. Wu, and W. A. Curtin, First-principles calculations of stacking fault energies in Mg-Y, Mg-Al, and Mg-Zn alloys and implications for $\langle c+a \rangle$ activity, Acta Mater. **136**, 249 (2017).
[76] A. Serra, D. J. Bacon, and R. C. Pond, The crystallography and core structure of twinning dislocations in H.C.P., Acta Metall. **36**, 3183 (1988).
[77] A. Serra, R. C. Pond, and D. J. Bacon, Computer simulation of the structure and mobility of twinning dislocations in H.C.P. metals, Acta Metall. Mater. **39**, 1469 (1991).
[78] A. Serra, D. J. Bacon, and R. C. Pond, Dislocation in interfaces in the H.C.P. metals–I. Defects formed by absorption of crystal dislocations, Acta Mater. **47**, 1425 (1999).
[79] D. J. Bacon, D. M. Barnett, and R. O. Scattergood, Anisotropic continuum theory of lattice defects, Prog. Mater. Sci. **23**, 51 (1980).
[80] J. E. Sinclair, P. C. Gehlen, R. G. Hoagland, and J. P. Hirth, Flexible boundary conditions and nonlinear geometric effects in atomic dislocation modeling, J. Appl. Phys. **49**, 3890 (1978).
[81] C. Woodward, First-principles simulations of dislocation cores, Mater. Sci. Eng. A **400-410**, 59 (2005).
[82] A. M. Z. Tan and D. R. Trinkle, Computation of the lattice Green function for a dislocation, Phys. Rev. E **94**, 023308 (2016).
[83] D. R. Trinkle, Lattice Green function for extended defect calculations: Computation and error estimation with long-range forces, Phys. Rev. B **78**, 014110 (2008).
[84] M. R. Fellinger, A. M. Z. Tan, L. G. Hector, Jr., and D. R. Trinkle, Geometries of edge and mixed dislocations in bcc Fe from first principles calculations, Phys. Rev. Materials **2**, 113605 (2018).
[85] G. Kresse, J. Furthmüller, and J. Hafner, *Ab initio* force constant approach to phonon dispersion relations of diamond and graphite, Europhys. Lett. **32**, 729 (1995).
[86] D. Alfè, G. D. Price, and M. J. Gillan, Thermodynamics of hexagonal-close-packed iron under earth's core conditions, Phys. Rev. B **64**, 45123 (2001).
[87] D. Alfè, Phon: A program to calculate phonons using the small displacement method, Comput. Phys. Commun. **180**, 2622 (2009).
[88] R. V. Kukta and K. Bhattacharya, A micromechanical model of surface steps, J. Mech. Phys. Sol. **50**, 615 (2002).
[89] C. R. Connell, R. E. Caflisch, E. Luo, and G. Simms, The elastic field of a surface step: The Marchenko-Parshin formula in the linear case, J. Comput. Appl. Math. **196**, 368 (2006).
[90] B. A. Szajewski, F. Pavia, and W. A. Curtin, Robust atomistic calculation of dislocation line tension, Modell. Simul. Mater. Sci. Eng. **23**, 085008 (2015).
[91] S. Plimpton, Fast parallel algorithms for short-range molecular dynamics, J. Comput. Phys. **117**, 1 (1995).
[92] LAMMPS Molecular Dynamics Simulator, http://lammps.sandia.gov (2021), accessed: 2021-07-23.